Heat flow analyses over Bornu Basin and its environs, Northeast Nigeria, using airborne magnetic and radiometric data: implication for geothermal energy prospecting

Taiwo Adewumi [1,2] · Kazeem Adeyinka Salako [2] · Alhassan Defyan Usman [2] · Emmanuel Emeka Udensi [2]

Abstract

The study presents the results of the analyses of heat flow for geothermal energy exploration on a reconnaissance basis within the Bornu Basin and its environs using an airborne magnetic and radiometric data set. The study area is bounded with latitude 11.00–13.00°N and longitude 11.00–14.00°E with an estimated total area of 72,600 km^2. The residual of the total magnetic field of the study area was subdivided into seventy-one (71) overlapping spectral blocks of 55 × 55 and 110 × 110 km^2 windows. Spectral analysis by fast Fourier transform was performed on each overlapping block, and centroid depth and depth to the top of the magnetic source were obtained from the plots of the log of energy against wave number. The results showed that the centroid depth for the two windows ranges from 6.28 to 17.70 km and 7.83 km to 23.50 km, respectively. Similarly, the depth to the top of the magnetic source for the two windows also ranges from 1.66 to 6.12 km and 2.27 km to 6.37 km. The Curie point depth obtained for the two windows ranges from 8.78 to 32.69 km and 10 km to 42 km, respectively. The heat flow obtained using an average thermal conductivity of 2.54 Wm^{-1}°C^{-1} ranges from 55.36 to 161.18 mWm^{-2} and 34.30 to 126 mWm^{-2} for the two windows, respectively. The maximum heat flow of 80 to 100 mWm^{-2} indicates that a geothermal potential source was found at the southeastern part of the study area corresponding to Gwoza and Galdekore. The results of radiogenic heat flow (RHP) range from 0.80 to 2.47 μWm^{-3}. The maximum RHP of 2.2 to approximately 2.5 μWm^{-3} is considered as radiometric signatures signifying probable geothermal potential sources, which could be found at the southeastern part of the study area corresponding to Gwoza and Galdekore. The agreement between the two heat flows obtained from the analysis of airborne magnetic and radiometric data sets is an indicator that the southeastern part of the study area is a viable source for potential geothermal energy exploration.

Keywords Airborne · Magnetic · Radiometric · Heat flow · Radiogenic · Geothermal energy · Spectral analysis

Introduction

Geophysical techniques are mostly integrated to determine the nature of the subsurface, investigate the subsurface layers and structures of the earth which might support hydrocarbon exploration, determine the heat flow from the earth's interior for geothermal exploration, delineate minerals and other economic materials present in the earth, and provide an integrated approach to some geological problems (Reynolds 2011). They are often used to complement the results from other geophysical methods adopted for particular research because different geophysical methods are sensitive to different physical properties of the subsurface media (rocks, sediment, water, void) (Reynolds 2011). High-resolution airborne magnetic and radiometric methods have been widely used by several scholars beyond geothermal exploration, such as mapping of subsurface geological structures (Anderson and Nash 1997; Bassey and Barka 2015; Okpoli and Akingboye 2016; Ejepu et al. 2018; Okeyode et al. 2019; Siagian et al. 2013; Ademila et al. 2019), mineral exploration (Goossens 1993; Airo 2007; Ercan et al. 2014; Appiah 2015; Adepelumi and Falade 2017; Eze et al. 2017; Elkhateeb and Abdellatif 2018; Pereira et al. 2019; Lawal 2020), and environmental monitoring and geological mapping (Paoletti and Pinto 2005; Ademila 2018).

✉ Taiwo Adewumi
    taiwo.adewumi@science.fulafia.edu.ng; tydon4real@yahoo.co.uk

[1] Department of Physics, Faculty of Science, Federal University of Lafia, Lafia, Nigeria

[2] Department of Geophysics, School of Physical Science, Federal University of Technology, Minna, Nigeria

The principal sources of heat flow from the earth's interior are derived from the cooling of the earth from its earlier hotter state during earth formation and the decay of radioactive isotopes, mainly from potassium, thorium, and uranium (Pollack and Chapman 1977; Benkhelil 1989; Vacquier 1998; Kearey et al. 2002). The decay of naturally occurring radioactive isotopes comes with the release of heat energy, and most of this is generated by the decay of ^{40}K, ^{238}U, and ^{232}Th (IAEA 2003). Rocks (sedimentary rocks) with a high concentration of ^{40}K, ^{238}U, and ^{232}Th that produce radiogenic heat flow and regions of shallow Curie point depths, high geothermal gradient, and high heat flow are the targets for geothermal prospecting in an area of investigation (Bansal et al. 2011; Alistair et al. 2014).

Previous heat flow studies carried out in the area of study include the following: Nwankwo and Ekine (2009) used well log data from fourteen oil wells in part of the Bornu Basin and obtained an average thermal conductivity of 2.35 $Wm^{-1}°C^{-1}$, and the heat flow results obtained ranged from 63.6 to 105.6 mWm^{-2} with an average of 80.6 mWm^{-2}. Kwaya et al. (2016) also carried out a heat flow analysis using well data from nineteen wells and obtained thermal conductivities ranging from 0.58 $Wm^{-1}K^{-1}$ to 4.207 $Wm^{-1}K^{-1}$ with an average of 1.626 $Wm^{-1}K^{-1}$ and heat flow ranging from 45 to 90 mWm^{-2}. Lawal and Nwankwo (2017), Akiishi et al. (2018), and Dimgba et al. (2020) used spectral analysis of aeromagnetic data and obtained heat flow values ranging from 33.23 to 79.76 mWm^{-2}, 89 to 117.80 mWm^{-2}, and 72.24 to 136.43 mWm^{-2}, respectively.

The present study attempts to combine airborne magnetic and radiometric methods to assess the heat flow over the Bornu Basin and its environs and provide an implication for geothermal exploration on a reconnaissance basis.

Location and the geologic settings of the study area

The area of study falls within the southwestern part of the Chad Basin, locally known as Bornu Basin, and its environs bounded by longitudes 11.00 to 14.00°E and latitudes 11.00 to 13.00°N in northeastern Nigeria with an estimated total area of 72,600 km^2 (Fig. 1). The study area is bordered by the Republic of Niger, Chad, and Cameroon to the north, northeast, and east, respectively.

The geology of the Bornu Basin has been discussed by different scholars, such as Okosun (1992 & 1995); Olugbemiro et al. (1997); Obaje (2009); and Olabode Solomon et al. (2015). The Bornu Basin falls in the southern part of the Chad Basin, which is one-tenth of the whole Chad Basin, which extends to the Niger Republic, Chad, and Cameroon. It forms part of the West-Central African rift system (WCAS) and was formed as a result of the mechanical division of the African crustal blocks in the Cretaceous (Genik

1992). The basin belongs to the West African rift system (WARS) component as WCAS (Okosun 1995). The Bornu Basin (study area) lies between latitudes 11.00 and 13.00°N and longitude 11.00 and 14.00°E, covering Borno State, part of Yobe State of Nigeria (Fig. 2).

Geologically, the Bornu Basin has been explained as a broad sediment-filled depression overlapping northeastern Nigeria and adjoining parts of the Republic of Chad (Obaje 2009). The sedimentary rocks of the area have a cumulative thickness of over 3.6 km, and the rocks consist of a thick basal continental sequence overlaid by transitional beds followed by a thick succession of Quaternary limnic, fluviatile, and eolian sands and clays.

The study area is made up of different formations (lithological units). The Chad formation, which is predominant in the area, occupies the northern and the eastern parts of the study area overlying other formations, the Keri-Keri formation at the southern and southwestern part overlying the Yolde formation at the southern part, the Pindiga formation at the southwestern part of the study area, the Gombe formation at the southwestern part overlain by the Chad formation, the Pindiga formation at the southern part intruded into the Chad formation, the Yolde at the extreme southern part, and the Bima formation overlain by the Keri-Keri formation at the southern part of the study area (Fig. 2).

Materials and methods

Data source

Twenty-four (24) half degrees by half degree airborne magnetic and radiometric data were acquired from the Nigerian Geological Survey Agency (NGSA) Abuja. The aero-radiometric and aeromagnetic data set were obtained as part of the airborne survey carried out between 2005 and 2009 by Fugro on behalf of the Nigerian Geological Survey Agency (NGSA 2005). The data were obtained at an altitude of 100 m along a flight line spacing of 500 m oriented in NW-SE and a tie line spacing of 2000 m. The maps are on a scale of 1:100,000 and half-degree sheets. The geomagnetic gradient was removed from the aeromagnetic data using the International Geomagnetic Reference Field (IGRF) of 2010.

Methods

The following steps were employed to achieve the aim and objectives of this study:

i. Assembling and knitting of the twenty-four aeromagnetic and aero-radiometric datasheets covering the study area to produce the total magnetic intensity (TMI) and the equivalent concentration maps of potassium (K), thorium (eTh),
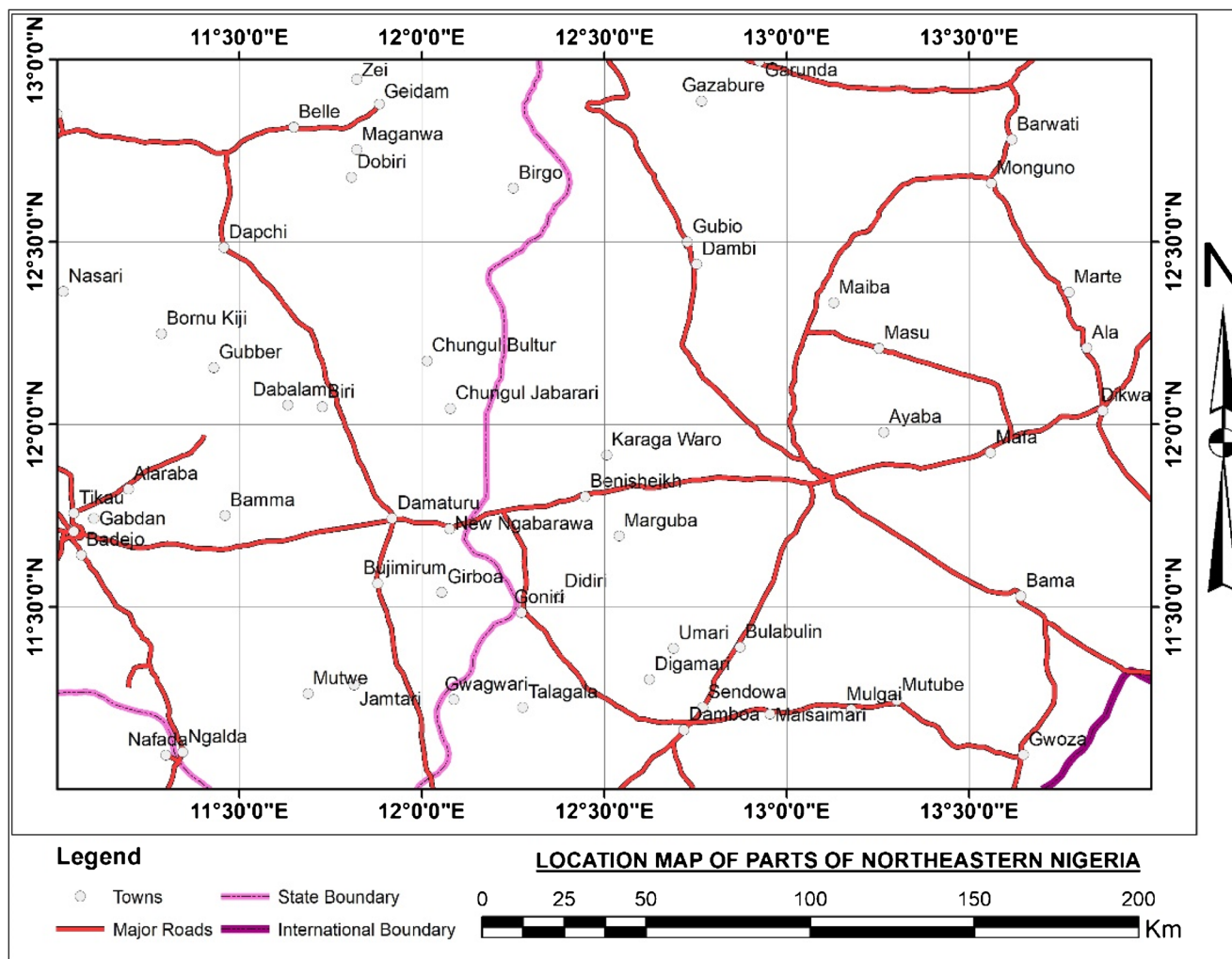
Fig. 1 Location map of the study area

and uranium (eU), respectively, using Oasis montaj software.

ii. Reduce the TMI map to the pole to get the exact position of the anomalies observed in the area over their causative bodies.

iii. Estimate the Curie point depth, geothermal gradient, and heat flow using a spectral analysis method.

iv. Determine radiogenic heat flow from the concentrations of potassium (K), uranium (eU), and thorium (eTh).

v. Using (iii) and (iv) to determine potential regions within the study area for geothermal prospecting.

Curie point depth, geothermal gradient, and heat flow from spectral method

The Curie point depth, geothermal gradient, and heat flow can be determined from the spectral analysis of the aeromagnetic data. The use of aeromagnetic data in determining

CPD has widely been used by several authors (Mayhew 1982, 1985; Okubo et al. 1985, 1989, 1991, Okubo and Matsunaga 1994, Okubo et al. 2003; Blakeley 1988; Tsokas et al. 1998; Salem et al. 2000, 2014; Bansal and Dimri 2010, Bansal et al. 2011; Abraham et al. 2014; Nwankwo and Shehu 2015; Irumhe et al. 2019; Dimgba et al. 2020). Spector and Grant (1970) explained the spectral analysis method which was used to determine the depth to the top of a magnetic four-sided prism (Z_t) from the gradient of the log of the power spectrum. The depth to centroid of the magnetized source rock (Z_o) was calculated by Bhattacharyya and Leu (1975, 1977) from the idea of Spector and Grant (1970). Okubo et al. (1985) combined and expanded the idea from Spector and Grant (1970) and Bhattacharyya and Leu (1977) to develop the method to determine the bottom depth of magnetized bodies (Z_b). If the degree at which a magnetic body of a 2D body is random and uncorrelated, the circular average of the power density spectra of the total field anomaly, p(k), could be
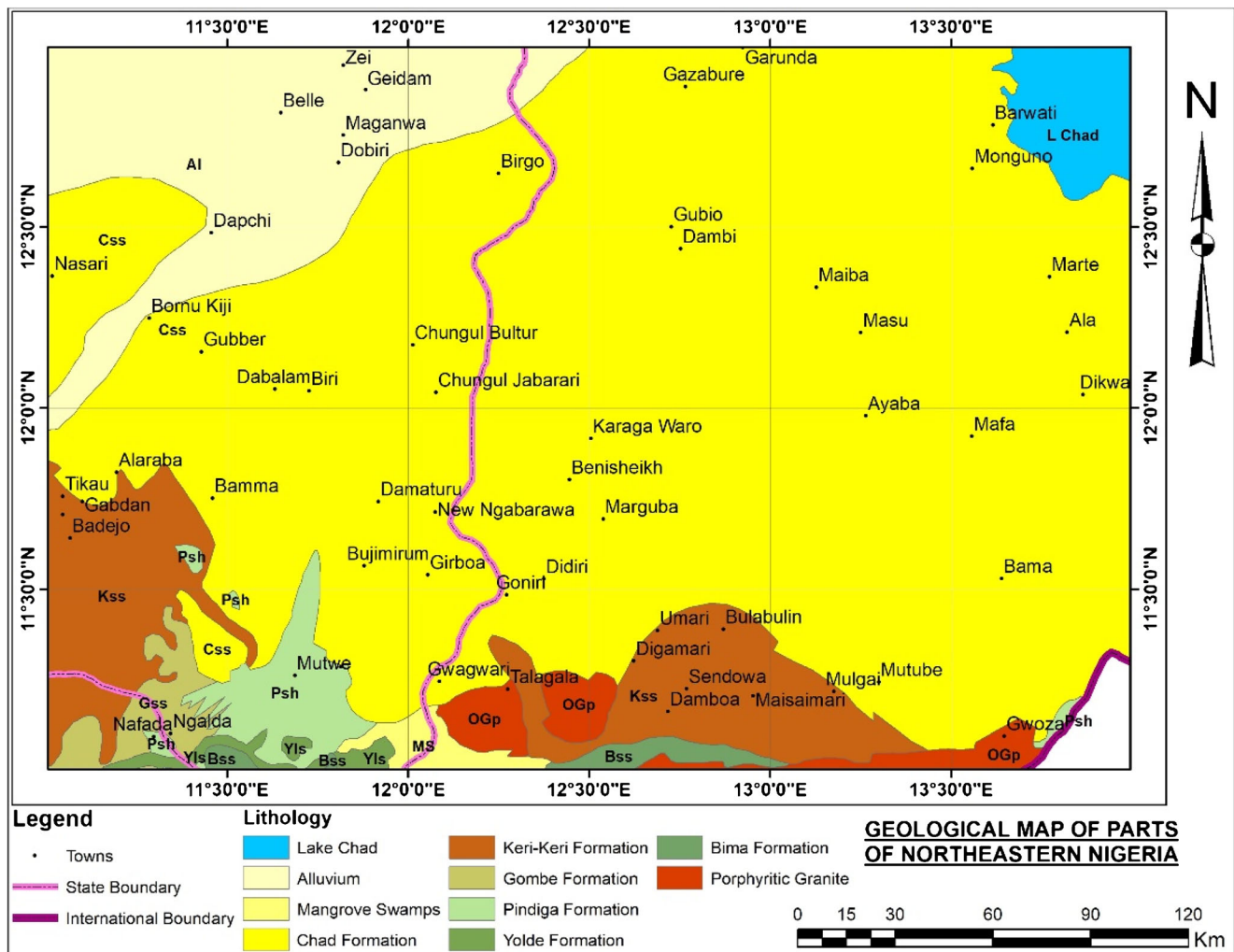
Fig. 2 Geological map of the study area

expressed as follows (Blakely 1995; Stampolidis et al. 2005; Bansal and Dimri 2010, Bansal et al. 2011; Salem et al. 2014):

$$P(k) = A|^{-2|k|Z_t} \left(1 - |^{-|k|(Z_b - Z_t)^2}\right) \qquad (1)$$

where A is considered to be a constant; Z_t and Z_b denote the depths to the top and bottom of the magnetic body, respectively; and k indicates the wave number of the magnetic field.

According to Okubo et al. (1985), depth to the bottom of magnetic bodies (Z_b) can be achieved in two stages. Firstly, the centroid depth (Z_o) of the deepest magnetic source is evaluated from the gradient of the longest wavelength part of the spectrum divided by the wave number using the following equation (Bansal et al. 2011; Nwankwo and Shehu 2015):

$$In\left(\frac{P(k)^{\frac{1}{2}}}{k}\right) = B - |k|Z_0 \qquad (2)$$

where P is the power spectral density, B is a constant quantity, and Z_o is the centroid depth.

Secondly, the uppermost depth to the magnetic body is also derived from the gradient of the high wave number portion of the power spectrum as follows:

$$In\left(P(k)^{\frac{1}{2}}\right) = C - 2|k|Z_t \qquad (3)$$

where P is the power spectral density, C is a constant quantity, and Z_t is the depth to top of the basement.

The depth to the bottom of magnetized body is therefore then obtained as follows:

$$Z_b = 2Z_0 - Z_t \qquad (4)$$

where Z_b is the depth to the bottom of the magnetized body, Z_o is the centroid depth, and Z_t is the depth to the top of magnetized body.

As earlier discussed, depth to the bottom of magnetic bodies was calculated in three phases: (i) dividing the residual map of the TMI map into overlapping blocks;

(ii) computing the logarithm of the power spectrum for each block, the centroid depth, and depth to the top of the magnetized body is obtained; and (iii) using $Z_b = 2Z_o - Z_t$, the basal depth is calculated.

Having calculated the DBMS, the heat flow is therefore calculated from the equation as follows:

$$q = k\frac{\partial T}{\partial Z} \tag{5}$$

where q is the heat flow, k is the thermal conductivity, and dT/dZ is the thermal gradient.

According to Tanaka et al. (1999); Stampolidis et al. (2005); and Maden (2010), the DBMS is related with the Curie temperature (580°C), and the vertical direction of temperature variation and the constant thermal gradient were assumed. The geothermal gradient (dT/dz) between the earth's surface and the Curie point depth (Zb) is defined using the relation as follows:

$$\frac{dT}{dz} = {\theta_c}/{z_b} \tag{6}$$

dT/dZ is the thermal gradient, $\theta c(580^o)$ is the Curie temperature, and Z_b is the Curie depth.

Application to aeromagnetic data

The spectral analysis was carried out on the residual field of the aeromagnetic anomaly data of the study area. The residual anomaly map was divided into seventy one (71) spectral overlapping square cells/blocks comprised of 44 blocks of 55×55 km^2 and 27 blocks of 110×110 km^2 for the spectral analysis. Of the spectral blocks, 50% overlapping was ensured in this study, and the choice of having the block division in two windows (55×55 km^2 and 110×110 km^2) was to avoid error in the interpretation of depth (Nwankwo and Shehu 2015). It is a tradition to subdivide the magnetic anomaly map into blocks/cell of choice dimension when performing spectral analysis. This has widely been done by several workers, for example. Connard et al. (1983) subdivided a total field magnetic anomaly map into overlapping blocks of 77×77 km^2 to determine the radially averaged power spectrum for each cell/block, Bektaş et al. (2007) divided residuals of the aeromagnetic anomaly map into 78 overlapping blocks of 150×150 km^2, and Shirani et al. (2020) also divided reduced to magnetic pole (RTP) of an aeromagnetic anomaly map into 55 overlapping blocks of 80×80 km^2 and determined the radially average power spectrum of each cell. Division of aeromagnetic anomaly maps into overlapping blocks of different dimensions is a choice of the interpreter of the aeromagnetic anomaly data. It is worth mentioning that Nwankwo and Shehu (2015) acknowledged the fact that the use of a small window size for the spectral analysis of aeromagnetic data

might be a fundamental error in the interpretation of aeromagnetic anomaly map for depth to the top of the magnetic basement.

In this study, the spectral analysis by FFT was performed on each overlapping block, and the plots of the logarithm of spectral energy ln(E) against the wave number (cycle/km) were produced using a Matlab program specifically designed to obtain the gradients for deepest depth (centroid depth) and depth to the top of a magnetic source.

Radiogenic heat production

Joly (1909) recognized the relationship between the observed heat flow and the heat generated by radioactive isotopes in local rocks. When a radioactive isotope decays, it emits energetic particles and gamma rays. The two particles that are important in radiogenic heat generation are alpha particles and beta particles. The alpha particles are equivalent to helium nuclei and are positively charged, while beta particles are electrons. To be a significant source of heat, a radioactive isotope must have a half-life comparable to the age of the earth, the energy of its decay must be fully converted to heat, and the isotope must be sufficiently abundant. All naturally occurring radioactive elements (NOREs) produce heat to a certain extent, but only the contributions of the decay series of ^{238}U, ^{234}U, ^{232}Th, and ^{40}K are geologically relevant (Vilà et al. 2010). The naturally occurring radioactive isotopes that produce heat, mainly ^{238}U, ^{234}U, ^{232}Th, and ^{40}K, are present in different concentrations in sedimentary rocks, and the heat production varies widely with lithology due to variations in the concentration of U, Th, and K (Haack 1982; Čermák and Rybach 1982). In natural uranium, the proportion of ^{238}U is 99.28%, ^{235}U is about 0.71%, and the rest is ^{234}U. The abundance of the radioactive isotope ^{40}K in natural potassium is only 0.01167%, but potassium is a very common element and its heat production is not negligible. The amounts of heat generated per second by these elements (in μWkg^{-1}) are uranium, 95.2; thorium, 25.6; and natural potassium, 0.00348 (Rybach 1988). The radioactive heat production (A in μWm^{-3}) by radioactivity in a rock that has concentrations C_U (ppm), C_{Th} (ppm), and C_K (%) for uranium, thorium, and potassium, respectively, is given as:

$$RHO = 10^{-5}\rho(9.52C_u + 2.56C_{Th} + 3.48C_k) \tag{7}$$

where RPH is the radioactive heat production in μWm^{-3}, ρ is the density of rocks, and C_U, C_{Th}, and C_K are concentrations for uranium, thorium, and potassium, respectively.

The radioactive heat contribution from the study area will be calculated from the concentration maps of uranium C_U, thorium C_{Th}, and potassium C_K using Eq. 7. The result obtained from this will be compared with the heat flow calculated from the spectral analysis of aeromagnetic data to ascertain

Fig. 3 Total magnetic intensity (TMI) map of the study area

Fig. 4 Residual of the total magnetic field of the study area

the source of heat within the area with implications on the geothermal resources within the study area.

Results and discussion

The TMI (Fig. 3) of the study area was subjected to regional/residual separation using polynomial fitting to remove the effects of the long-wavelength anomalies that might overshadow anomalies of interest. The residual map of the study area (Fig. 4) is characterized by high (positive) and low (negative) magnetic anomalies with the magnetic values ranging from −132.1 to 159.2 nT. The sum of 33,000 nT removed from the total magnetic field for the purpose of handling must be added to it to get the actual value of the total magnetic field at any point. Variations of magnetic signature in the earth's magnetic field are produced from three major sources: variation in the lithologic units, basement structures, and authigenic minerals in sedimentary rocks (Bird 1997). Dominant

structures delineated on the map trend NE-SW which is related to the Pan African trend (Okosun 1995; Aderoju et al. 2016). Other structures identified on the map trend E-W and NW-SE.

This map was used for the spectral analysis to estimate the Curie depth, geothermal gradient, and heat flow for potential geothermal prospecting sites within the study area.

Interpretation of Curie point depth, geothermal gradient, and heat flow maps

The depth to the bottom of the magnetic source (Curie point depth) was determined from the centroid depth (Z_o) and depth to top of the magnetic basement (Z_t) using Eq. 4 ($Z_b = 2Z_o - Z_t$). The Z_o and the Z_t were obtained from the plots of the logarithm of spectral power density (lnP) against the wave number (Fig. 5a, b, c, d). Table 1 presents the calculated centroid depth and depth to top of basement obtained from blocks 55×55 km^2 range from 7.83 to 23.5 km and 2.44 to 6.37 km, respectively. Table 2 presents the results of centroid depth and

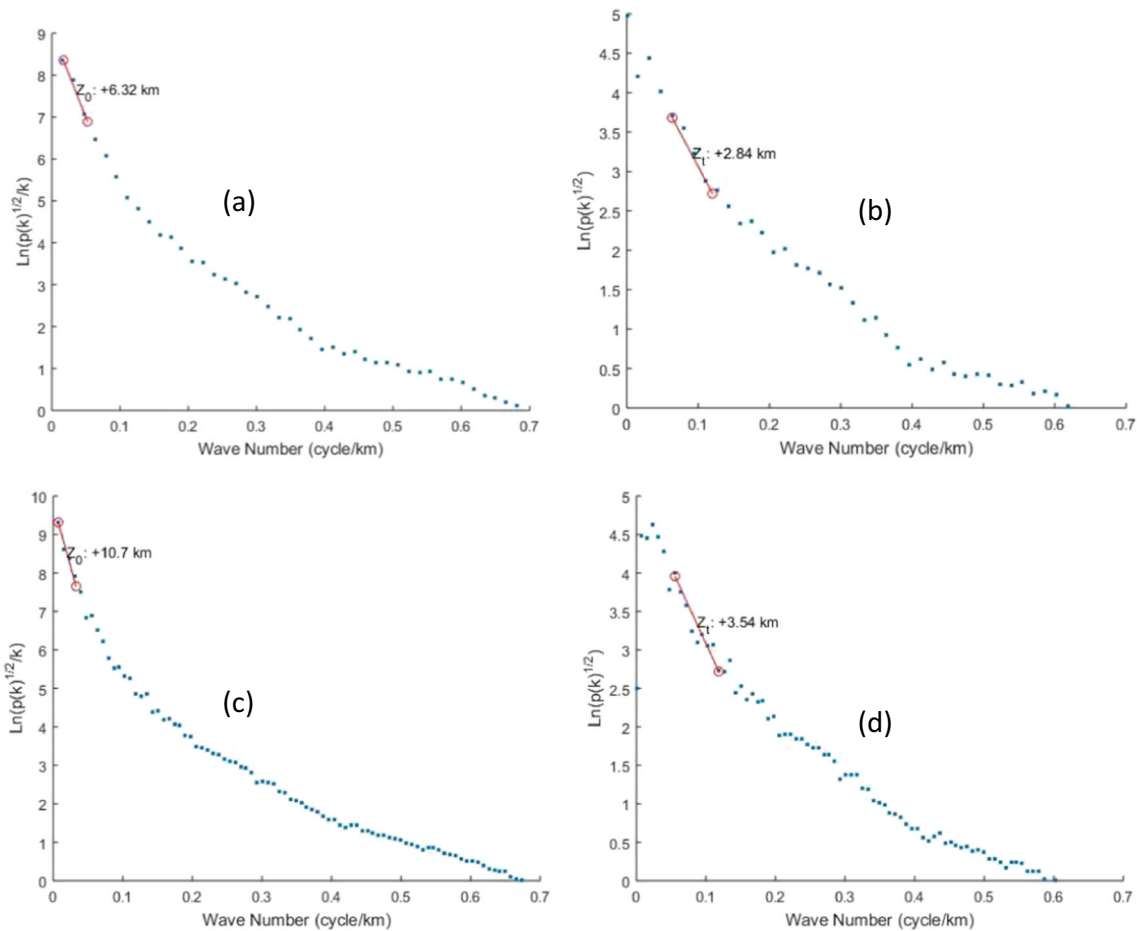**Fig. 5** **a** Spectral plot of block 1 (55×55 km^2) showing the centroid depth (Z_o). **b** Spectral plot of block 1 (55×55 km^2) showing the depth to top of basement. **c** Spectral plot of block 1 (110×110 km^2) showing the centroid depth. **d** Spectral plot of block 1 (110×110 km^2) showing the depth to top of basement

Table 1 Spectral results of the estimation of the CPD, geothermal gradient, and heat flow of the study area (blocks 55 × 55 km²)

Block nos	Longitude (°)	Latitude (°)	Centroid depth (km)	Depth to top (km)	CPD (km)	Geothermal Gradient (C/km)	Heat flow (mW/m²)
1	11.25	12.75	6.32	2.84	9.8	59.18	150.32
2	11.50	12.75	17.70	2.71	32.69	17.74	45.06
3	11.75	12.75	8.10	5.55	10.65	54.46	138.32
4	12.00	12.75	9.76	2.41	17.11	33.898	86.10
5	12.25	12.75	7.90	2.00	13.8	42.02	106.75
6	12.50	12.75	7.67	3.19	12.15	47.73	121.25
7	12.75	12.75	7.34	2.93	11.75	49.36	125.37
8	13.00	12.75	6.90	3.85	9.95	58.29	148.06
9	13.25	12.75	8.04	3.59	12.49	46.43	117.95
10	13.50	12.75	10.30	3.07	17.53	33.08	84.03
11	13.75	12.75	7.25	5.30	9.2	63.04	160.130
12	11.25	12.25	8.18	2.52	13.84	41.90	106.44
13	11.50	12.25	8.77	3.40	14.14	41.01	104.18
14	11.75	12.25	8.07	2.72	13.42	43.21	109.77
15	12.00	12.25	9.06	2.06	16.06	36.11	91.73
16	12.25	12.25	6.87	3.50	10.24	56.64	143.86
17	12.50	12.25	10.10	4.49	15.71	36.91	93.77
18	12.75	12.25	11.70	3.83	19.57	29.63	75.27
19	13.00	12.25	16.20	5.32	27.08	21.41	54.40
20	13.25	12.25	10.00	5.63	14.37	40.36	102.51
21	13.50	12.25	14.50	5.32	23.68	24.49	62.21
22	13.75	12.25	6.28	3.78	8.78	66.05	167.79
23	11.25	11.75	6.90	2.49	11.31	51.28	130.25
24	11.50	11.75	10.30	4.14	16.46	35.23	89.50
25	11.75	11.75	7.91	2.75	13.07	44.37	112.71
26	12.00	11.75	7.97	2.63	13.31	43.57	110.68
27	12.25	11.75	8.88	1.66	16.1	36.02	91.50
28	12.50	11.75	11.20	1.93	20.47	28.33	71.96
29	12.75	11.75	10.40	3.65	17.15	33.81	85.90
30	13.00	11.75	14.60	3.15	26.05	22.26	56.55
31	13.25	11.75	10.10	4.27	15.93	36.40	92.47
32	13.50	11.75	14.60	2.59	26.61	21.79	55.36
33	13.75	11.75	13.10	1.72	24.48	23.69	60.17
34	11.25	11.25	9.06	3.6	14.52	39.94	101.46
35	11.50	11.25	7.17	3.51	10.83	53.55	136.02
36	11.75	11.25	13.80	6.12	21.48	27.00	68.58
37	12.00	11.25	7.80	2.62	12.98	44.68	113.49
38	12.25	11.25	11.10	3.01	19.19	30.22	76.76
39	12.50	11.25	11.40	3.58	19.22	30.17	76.64
40	12.75	11.25	10.30	4.24	16.36	35.45	90.04
41	13.00	11.25	11.20	4.69	17.71	32.74	83.18
42	13.25	11.25	7.05	4.96	9.14	63.45	161.18
43	13.50	11.25	8.56	2.43	14.69	39.48	100.28
44	13.75	11.25	6.40	2.14	10.66	54.40	138.19

depth to top of basement blocks 110 × 110 km² ranging from 6.28 to 17.7 km and 1.66 to 6.12 km, respectively. The Curie point depth (CPD) determined from the spectral blocks of 55 × 55 km² ranges from 8.78 to 32.69 km. The contour map of the CPD of spectral blocks of 55 × 55 km² (Fig. 6a) shows that the maximum CPD is located at the northwestern and central to

Table 2 Spectral results of the estimation of the CPD, geothermal gradient, and heat flow of the study area (blocks 110 ×110 km^2)

Block nos	Longitude (°)	Latitude (°)	Centroid depth (km)	Depth to top (km)	CPD (km)	Geothermal gradient (°C/km)	Heat flow (mW/m^2)
1	11.50	12.50	10.70	3.54	17.86	32.47	82.48
2	11.75	12.50	12.50	4.20	20.8	27.88	70.82
3	12.00	12.50	14.10	4.01	24.19	23.97	60.90
4	12.25	12.50	16.80	3.79	29.81	19.45	49.41
5	12.50	12.50	12.80	3.93	21.67	26.76	67.98
6	12.75	12.50	19.00	4.07	33.93	17.09	43.41
7	13.00	12.50	18.80	5.58	32.02	18.11	46.00
8	13.25	12.50	18.40	5.78	31.02	18.69	47.49
9	13.50	12.50	20.50	5.09	35.91	16.15	41.02
10	11.50	12.00	14.80	2.44	27.16	21.35	54.24
11	11.75	12.00	22.60	2.49	42.71	13.57	34.49
12	12.00	12.00	20.40	2.81	37.99	15.26	38.77
13	12.25	12.00	19.30	2.76	35.84	16.18	41.10
14	12.50	12.00	13.30	3.19	23.41	24.77	62.93
15	12.75	12.00	20.50	5.32	35.68	16.25	41.28
16	13.00	12.00	13.90	6.37	21.43	27.06	68.74
17	13.25	12.00	21.50	4.79	38.21	15.17	38.55
18	13.50	12.00	13.60	4.80	22.4	25.89	65.76
19	11.50	11.50	13.40	3.31	23.49	24.69	62.71
20	11.75	11.50	22.90	2.85	42.95	13.50	34.30
21	12.00	11.50	8.18	2.27	14.09	41.16	104.55
22	12.25	11.50	18.60	2.97	34.23	16.94	43.03
23	12.50	11.50	8.06	2.70	13.42	43.21	109.77
24	12.75	11.50	23.20	4.90	41.5	13.97	35.49
25	13.00	11.50	10.10	3.38	16.82	34.48	87.58
26	13.25	11.50	23.50	5.18	41.82	13.86	35.22
27	13.50	11.50	7.83	4.01	11.65	49.78	126.45

the eastern part of the study area corresponding to Guba, Buruta, Shettimari; Kilborani, Kesangala, Zunfur, Maiba, Gabchari, and Galtaru and Marte, Alla, Kariari, and Dikwa, respectively. The minimum CPD value was found at the SE, NE, extreme NW, and northern part of the study area corresponding to Jongo, Ngrabawa, Galdekore, Nugurosoye, and Bama; Mintur, Ngelewa, and Kukawa; Gazabure; and Garunda, respectively. The contour map of the CPD obtained from the spectral blocks of 110 × 110 km^2 (Fig. 6b) reveals CPD values ranging from 10 to 42 km with maximum values found at the central western part corresponding to Shegau, Babban Gida, Dabalam, Biri, and Masho; at central SW part corresponding to Ngelzarma, Garin Basam, Bolkolo, Gujba, and N. Fulani; at the central-eastern part corresponding to Bolori, Gongolon, Ayaba, and Masu; and at the NE part corresponding to Mintur, Ngelewa, and Karba. The minimum values were found at the NW corresponding to Gashua; at the extreme western part corresponding to Nasari; at the extreme SW part corresponding to Kadi; at the SE part corresponding to Bama, Shigabaja, Galdekore, Nugurosoye, and Gwoza.

Curie point depths vary with geological situations (Ross et al. 2006). Tanaka et al. (1999) established that CPD ranging below 10 km is attributable to volcanic and geothermal regions, 10 to 15 km is attributable to island arch and ridges, 20 km and above is attributable to plateaus, and 30 km and above is attributable to trenches.

The geothermal gradient of the study area was produced and presented by Fig. 6c and Fig. 6d for each spectral block of 55 × 55 km^2 and 110 × 110 km^2, respectively, using a Curie temperature of 580°C. The geothermal gradient ranges from 20 to 68 °C.km^{-1} and 12 to 50 °C.km^{-1} for the spectral blocks of 55 × 55 km^2 and 110 × 110 km^2, respectively.

The heat flow was produced for the each of the spectral blocks of 55 × 55 km^2 and 110 × 110 km^2 using an average thermal conductivity of 2.54 W/m°C obtained from the study area by Dieokuma et al. (2013). Figure 6e and Fig. 6f show that the heat flow obtained for each spectral block of 55 × 55 km^2 and 110 × 110 km^2 ranges from 55.36 to 161.18 mWm^{-2} and 34.30 to 126 mWm^{-2}, respectively. The results of the heat flow are inversely proportional to that of CPDs, with the
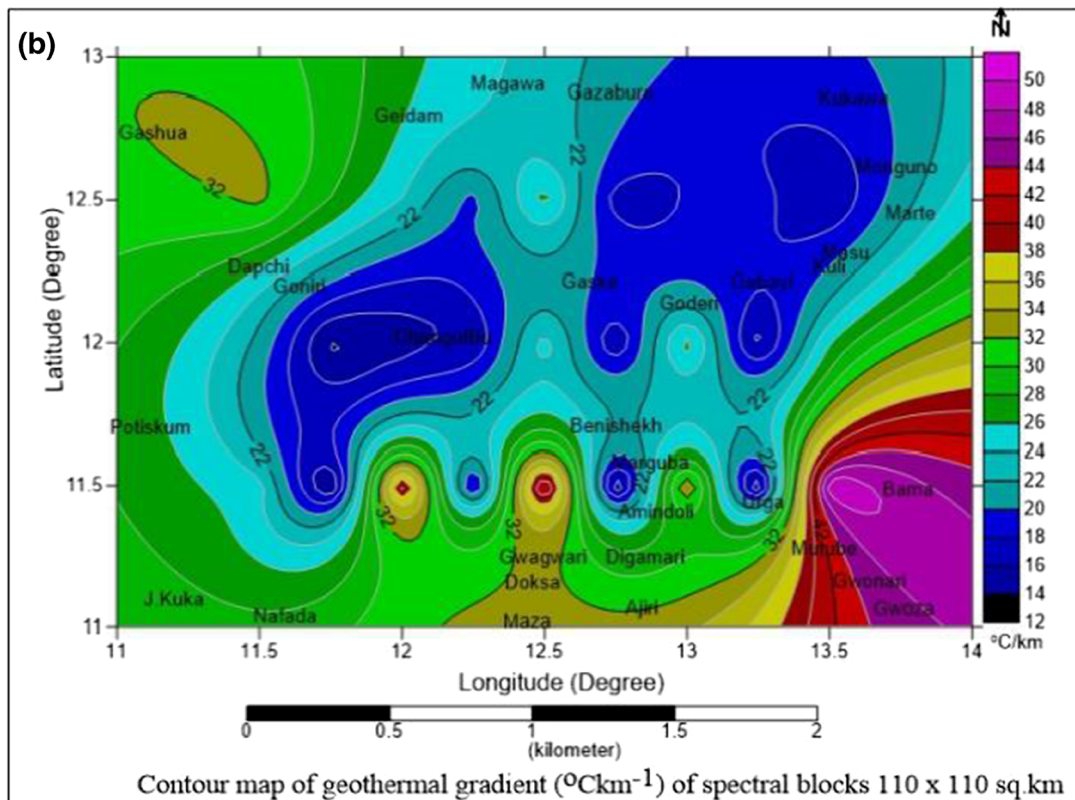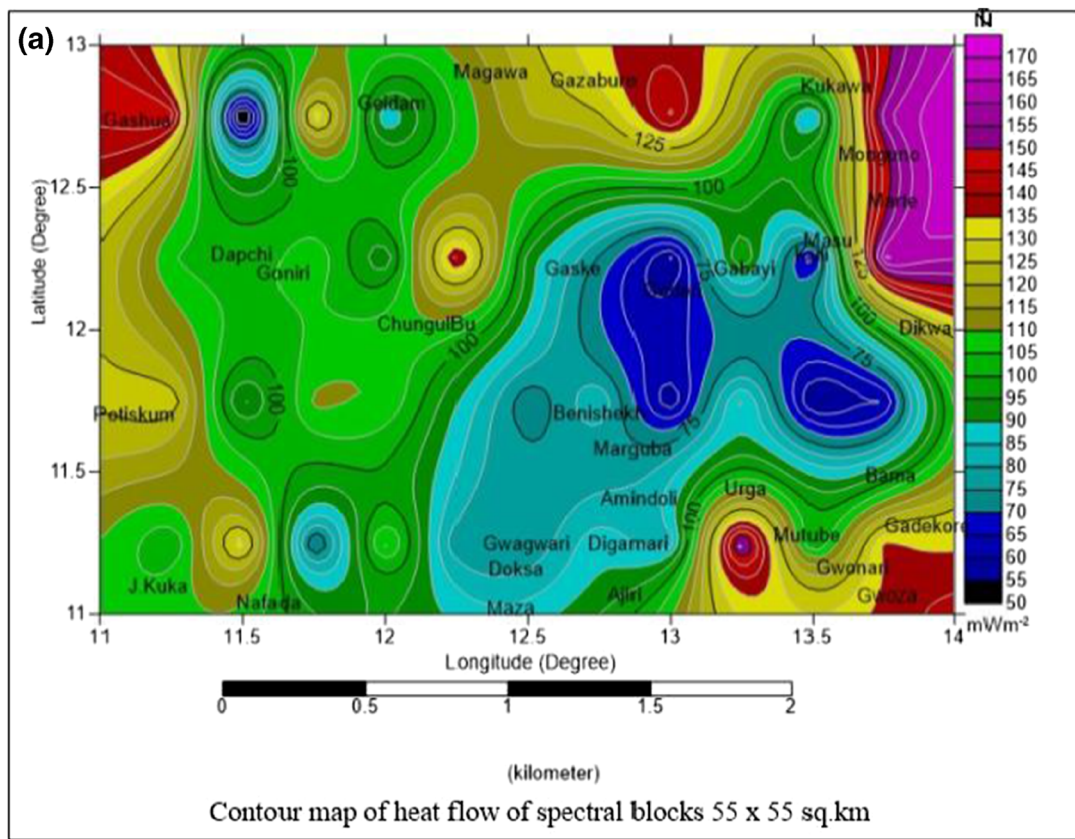
Fig. 6 **a** Contour map of CPD of spectral blocks 55×55 km^2. **b** Contour map of CPD of spectral blocks 110×110 km^2. **c** Contour map of geothermal gradient (°C/km) of spectral blocks 55×55 km^2. **d** Contour map of geothermal gradient (°C/km) of spectral blocks 110×110 km^2. **e** Contour map of heat flow of spectral blocks 55×55 km^2. **f** Contour map of heat flow of spectral blocks 110×110 km^2
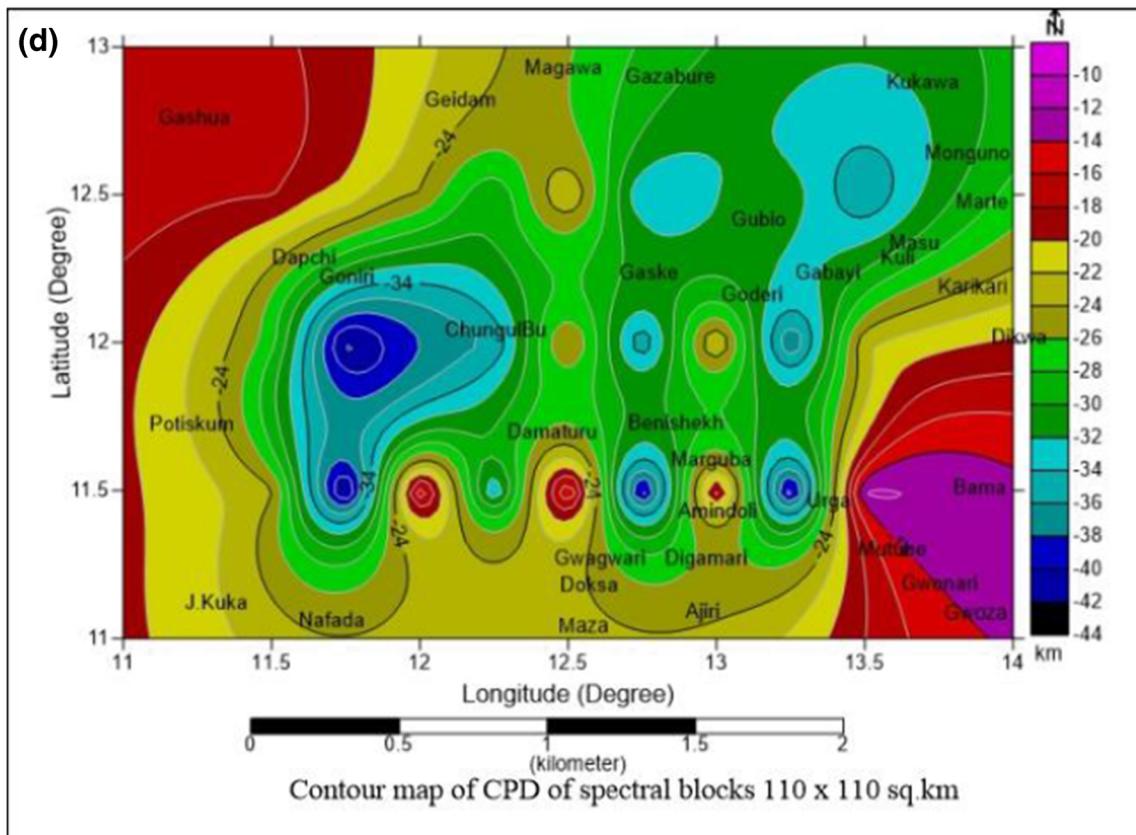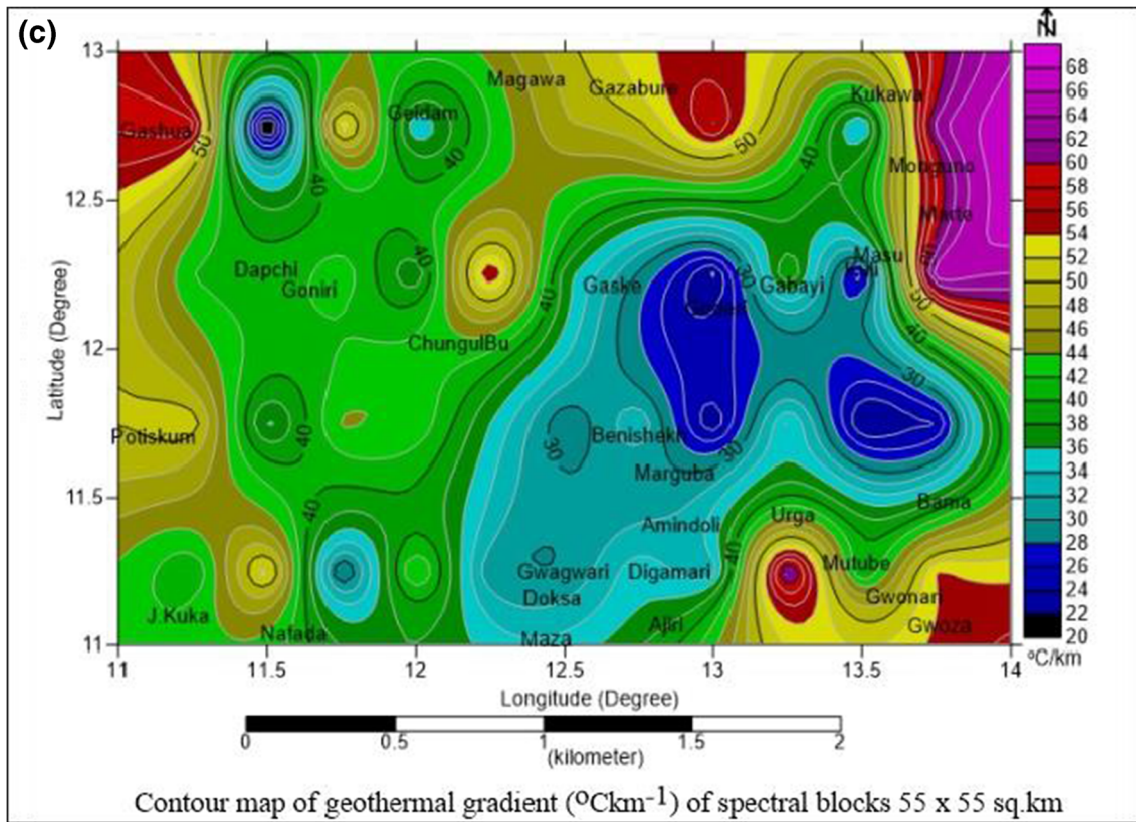
Contour map of geothermal gradient (°Ckm^{-1}) of spectral blocks 55 x 55 sq.km

Contour map of CPD of spectral blocks 110 x 110 sq.km

Fig. 6 (continued)

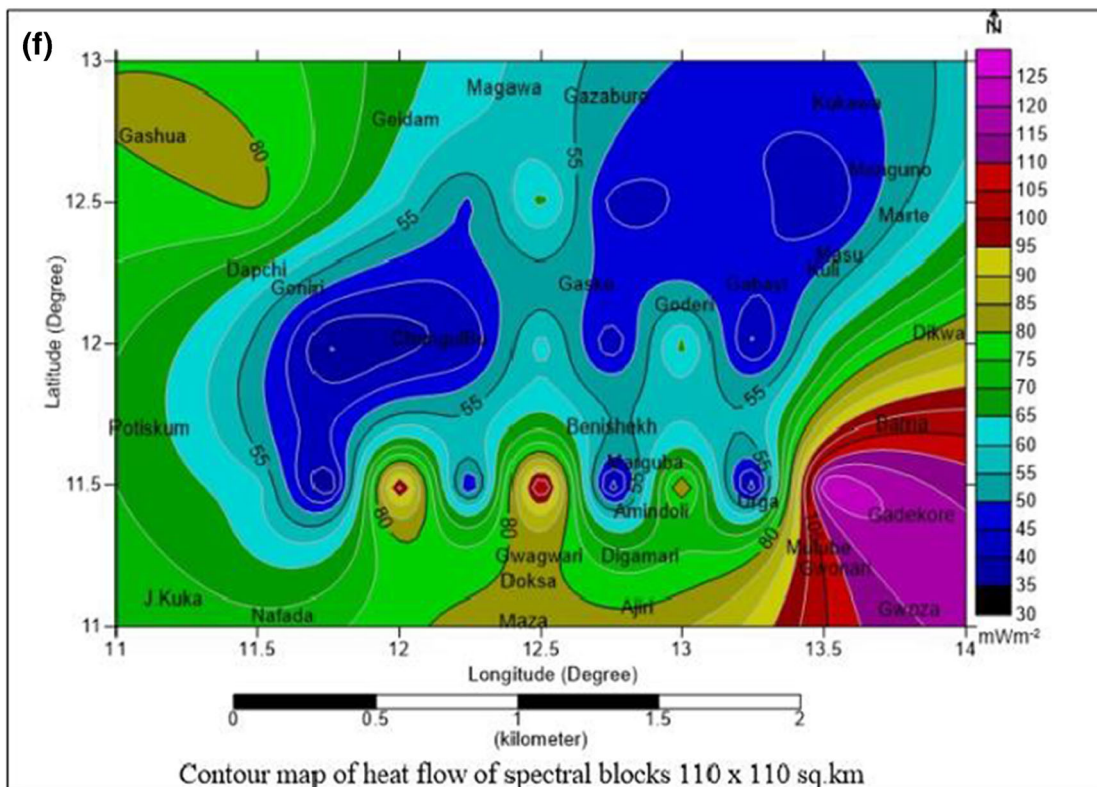Contour map of CPD of spectral blocks 55 x 55 sq.km

Contour map of heat flow of spectral blocks 110 x 110 sq.km

Fig. 6 (continued)

(a)

Equivalent Potassium (K%) Concentration Map

(b)

Equivalent Thorium (eTh) Concentration Map
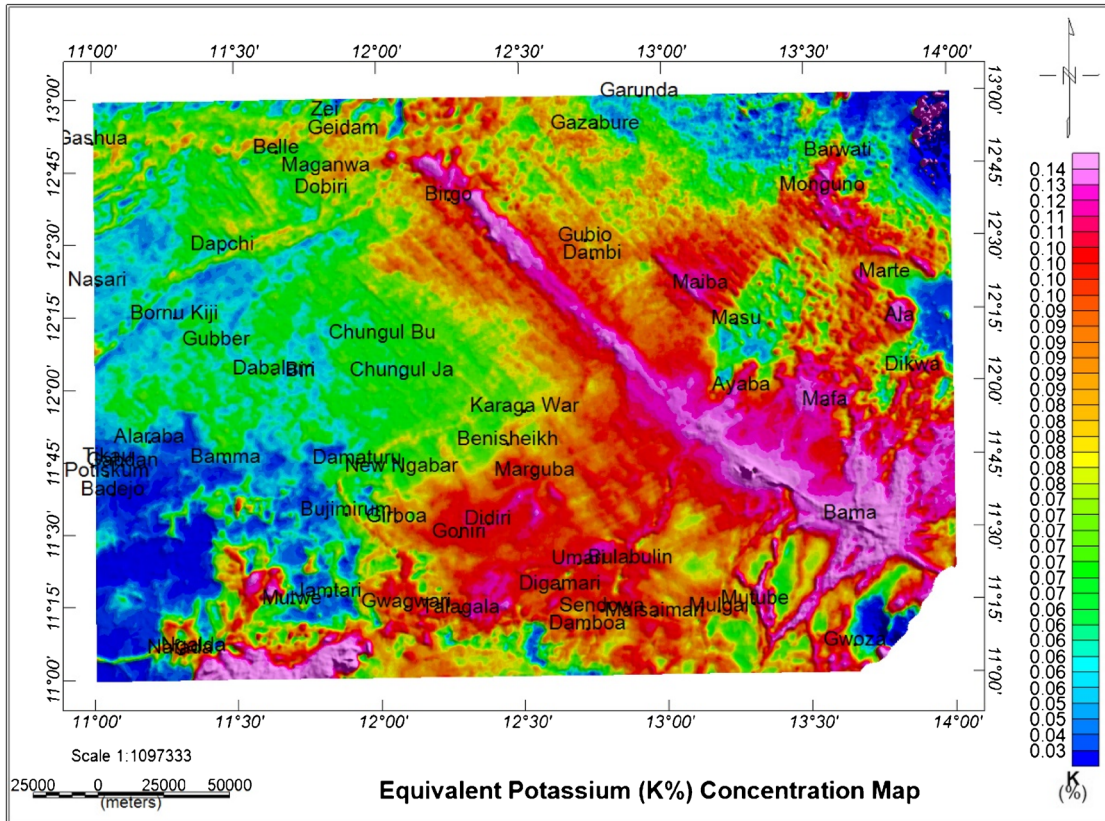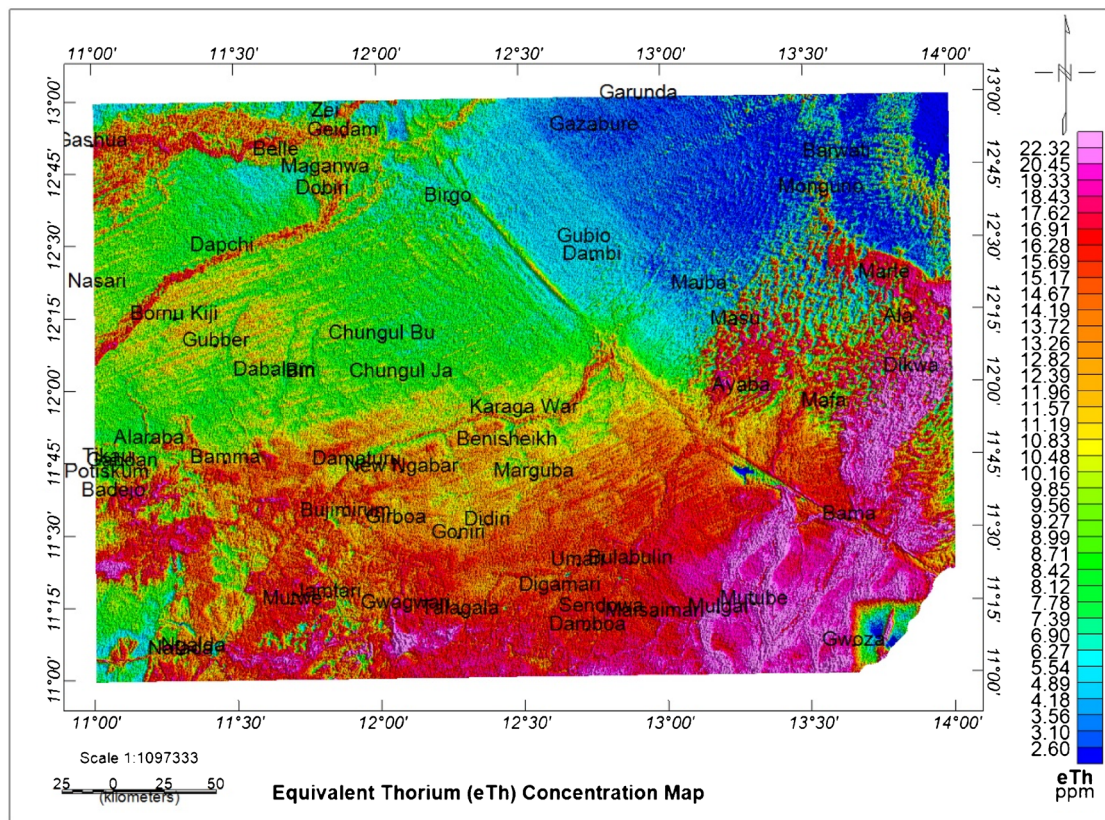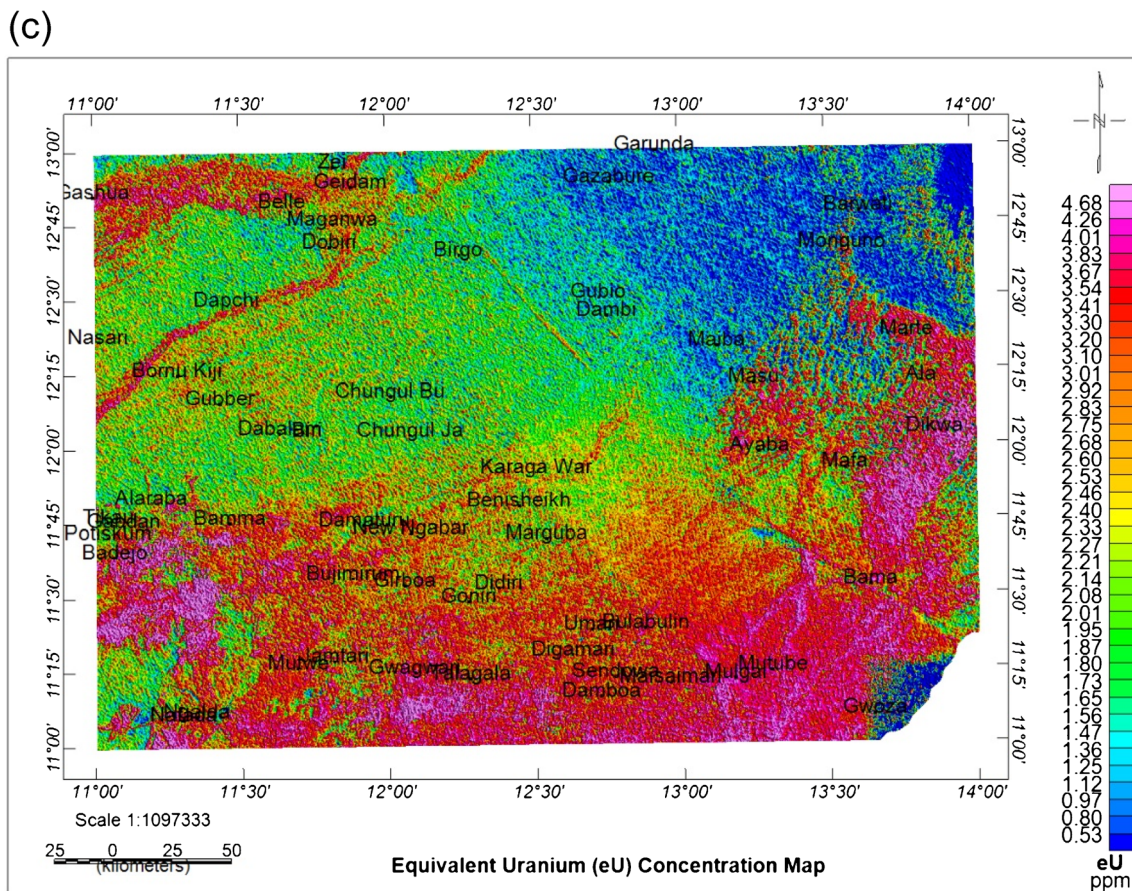
(c)
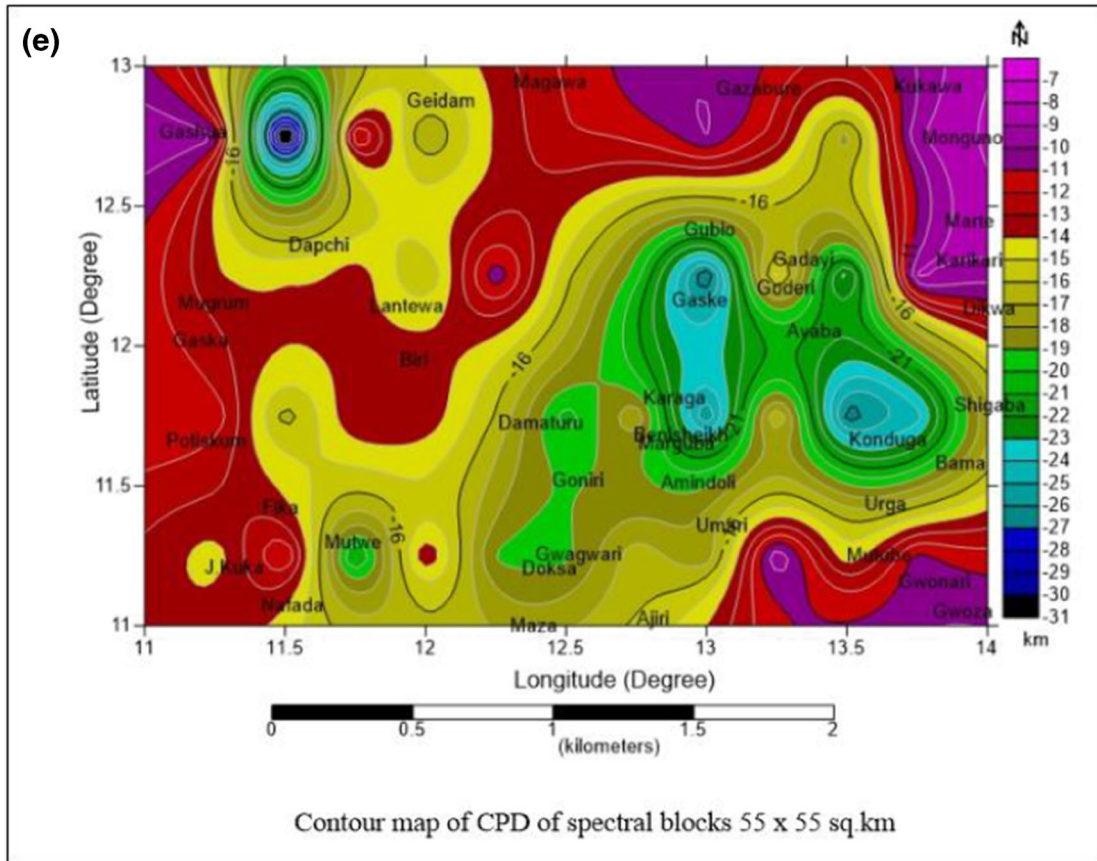
Fig. 7 **a** Potassium concentration (K %) map of the study area. **b** Equivalent thorium (eTh) concentration map of the study area. **c** Equivalent uranium (eU) concentration map of the study area

region of high heat flow corresponding to regions of shallow CPD. An average of heat flow in the terrestrial continental crust was between 65 and 48 mWm^{-2} (Abraham et al. 2014). The heat flow value between 80 and 100mWm^{-2} has been established to indicate geothermal anomalous conditions in an area for geothermal prospecting (Jessop et al. 1984). It can therefore be deduced from this study that there are good spots for geothermal energy resources such as the NW, southern, SE, central, eastern, and NE part of the study area. It is worth noting that the blocks in 110 × 110 km^2 yield a better result for the CPD and the heat flow vis-à-vis the ones of 55 × 55 km^2. This result agreed with the previous work in the study area (Nwankwo et al. 2009; Kwaya et al. 2016; Akiishi et al. 2018; Dimgba et al. 2020).

Interpretation of uranium (eU), thorium (eTh), and potassium (K) concentration maps

Figure 7a, b, and c are the gamma-ray spectrometric maps that emphasize the nature of the radioelement distribution and are thus suited to the recognition of the geological features within the study area. These maps (K, eTh, and eU) are characterized by high, intermediate, and low concentrations and also reveal a general relation to the rock units in the study area. Figure 7a shows a high concentration of potassium at the southeastern part, southern part, and the eastern part corresponding to Bama, Mutube, and Damboa; Nafada; and Dikwa, Mafa, and Ayaba, respectively. It also shows that the intermediate concentration could be found at the central, western, and northwestern part corresponding to Chungul Bu, Karaga, and Benisheikh; Nasari, Potiskum, Badejo, and Alaraba; and Gashua, Nasari, Dapchi, and Bornu Kiji, respectively. The low concentration occurred in the northern part and northeastern part corresponding to Gazabure and Monguno, respectively. The concentration value of potassium ranges from 0.12 to 2.70%. Figure 7b and c are the equivalent thorium and uranium concentration maps, respectively. The equivalent thorium and uranium concentration values ranged from 2.60 to 22.32 ppm and 0.53 to 4.68 ppm, respectively. A close inspection of these maps shows that the regions of high, intermediate, and low concentrations correlate with Fig. 7a. This shows that the three radioelements have the same distribution in the study area.

Table 3 The summary of the mean concentration of eU (ppm), eTh (ppm), K (%), TC, and the RHP (μWm^{-3})

Profile no	Long. (°E)	Lat. (°N)	Mean C_u (ppm)	Mean C_{Th} (ppm)	Mean C_k (%)	Mean Total count	RHP (μWm^{-3})
N-S01	11.07	12.00	2.70	11.10	0.60	14.40	1.46
N-S02	11.18	12.00	2.60	10.90	0.60	14.10	1.42
N-S03	11.28	12.00	2.80	11.40	0.60	14.80	1.50
N-S04	11.41	12.00	2.50	10.50	0.70	13.70	1.38
N-S05	11.55	12.00	2.60	11.50	0.90	150	1.49
N-S06	11.71	12.00	2.60	11.60	0.70	14.90	1.47
N-S07	11.99	12.00	2.50	10.70	0.80	140	1.40
N-S08	12.11	12.00	2.50	11.20	0.90	14.60	1.44
N-S09	12.32	12.00	2.30	10.60	0.90	13.80	1.35
N-S10	12.52	12.00	2.20	9.70	0.90	12.80	1.27
N-S11	12.72	12.00	2.20	9.90	0.90	130	1.28
N-S12	12.93	12.00	2.20	9.90	1.00	13.10	1.29
N-S13	13.08	12.00	2.20	10.10	0.90	13.20	1.29
N-S14	13.35	12.00	2.40	12.90	1.20	16.50	1.56
N-S15	13.58	12.00	2.60	13.30	1.40	17.30	1.65
N-S16	13.70	12.00	2.50	12.40	1.40	16.30	1.5
N-S17	13.75	12.02	2.50	13.60	1.40	17.50	1.65
N-S18	13.8	12.07	2.50	13.60	1.40	17.50	1.65
N-S19	13.87	12.12	2.50	13.30	1.20	17.00	1.61
N-S20	13.95	12.19	2.30	12.30	0.80	15.40	1.46
E-W01	12.49	12.93	1.60	6.40	0.30	8.30	0.84
E-W02	12.49	12.74	1.50	6.10	0.30	7.90	0.80
E-W03	12.49	12.58	1.60	6.40	0.30	8.30	0.84
E-W04	12.47	12.43	1.80	7.90	0.30	1.00	0.99
E-W05	12.49	12.27	2.10	9.30	0.20	11.60	1.15
E-W06	12.48	12.09	2.30	10.80	0.30	13.40	1.31
E-W07	12.49	11.99	2.50	11.70	0.50	14.70	1.44
E-W08	12.50	11.81	2.60	12.40	0.60	15.60	1.52
E-W09	12.51	11.64	3.10	14.20	0.60	17.90	1.76
E-W10	12.49	11.53	3.10	14.80	0.70	18.60	1.81
E-W11	12.49	11.39	3.30	16.10	0.80	20.20	1.96
E-W12	12.45	11.35	3.40	16.20	0.80	20.40	1.99
E-W13	12.44	11.24	3.00	15.40	0.70	19.10	1.83
E-W14	12.4	11.18	3.20	15.70	0.70	19.60	1.90
E-W15	12.36	11.09	3.60	17.40	0.70	21.70	2.11
NE-SW01	11.09	12.87	2.80	11.30	0.80	14.90	1.51
NE-SW02	11.25	12.63	2.30	9.80	0.60	12.70	1.27
NE-SW03	11.42	12.39	2.20	9.30	0.60	12.10	1.21
NE-SW04	11.63	12.19	2.60	10.70	0.60	13.90	1.41
NE-SW05	11.8	12.15	2.40	9.60	0.60	12.60	1.28
NE-SW06	11.93	12.12	2.30	9.20	0.50	12.00	1.22
NE-SW07	12.07	12.04	2.10	8.30	0.50	10.90	1.11
NE-SW08	12.23	12.02	2.10	8.40	0.50	11.00	1.12
NE-SW09	12.42	12.02	1.90	8.30	0.60	10.80	1.07
NE-SW10	12.56	12.00	2.10	9.10	0.70	11.90	1.18
NE-SW11	12.77	11.99	2.00	9.00	0.80	11.80	1.16
NE-SW12	13.03	11.81	2.70	13.00	1.20	16.90	1.64
NE-SW13	13.33	11.65	3.10	15.90	1.40	20.40	1.95

Profile no	Long. (°E)	Lat. (°N)	Mean C_u (ppm)	Mean C_{Th} (ppm)	Mean C_k (%)	Mean Total count	RHP (μWm^{-3})
NE-SW14	13.45	11.53	3.80	20.20	2.10	26.10	2.47
NE-SW15	13.72	11.44	3.40	18.60	2.20	24.20	2.27

Interpretation of estimated radiogenic heat production from the mean concentration of U, Th, and K

The radiogenic heat production (RHP) was calculated from the mean concentration of naturally occurring radioactive isotopes (U, Th, and K) of the study area using Eq. 7 (Rybach 1986). Fifty profiles were drawn (in N-S, E-W, and NE-SW direction) on the concentration maps (Fig. 7a, b, c) of the three naturally occurring radioactive elements (U, Th, and K) to obtain the mean values of each element for the calculation of the radiogenic heat production. Table 3 presents the summary of the mean values of the concentrations for uranium, thorium, potassium, total count, and the estimated radiogenic heat production obtained from the study area. The mean concentration for U, Th, and K ranges from 1.50 to 3.80 ppm, 6.10 to 17.40 ppm, and 0.20 to 2.20%, respectively. The estimated RHP ranged from 0.80 to 2.47 μWm^{-3}. The contour map (Fig. 8) of the RHP shows that the maximum RHP of 2.2 to approximately 2.5 μWm^{-3} is found at the southeastern part of the study area, corresponding to Gwoza and Galdekore.

A previous study such as Rybach and Buntebarth (1981) has recorded the mean of radiogenic heat flow as 2.25 μWm^{-3} for younger sedimentary and granitic rocks. Higher values are considered as radiometric signatures signifying probable geothermal potential sources that are only crustal in origin without contribution from the mantle. Radiogenic heat production in sediments depends on significant conditions that affect their thermal history and the heat flow in the basin (Rybach 1986). It can therefore be inferred from the results obtained that the southeastern part of the study area corresponding to
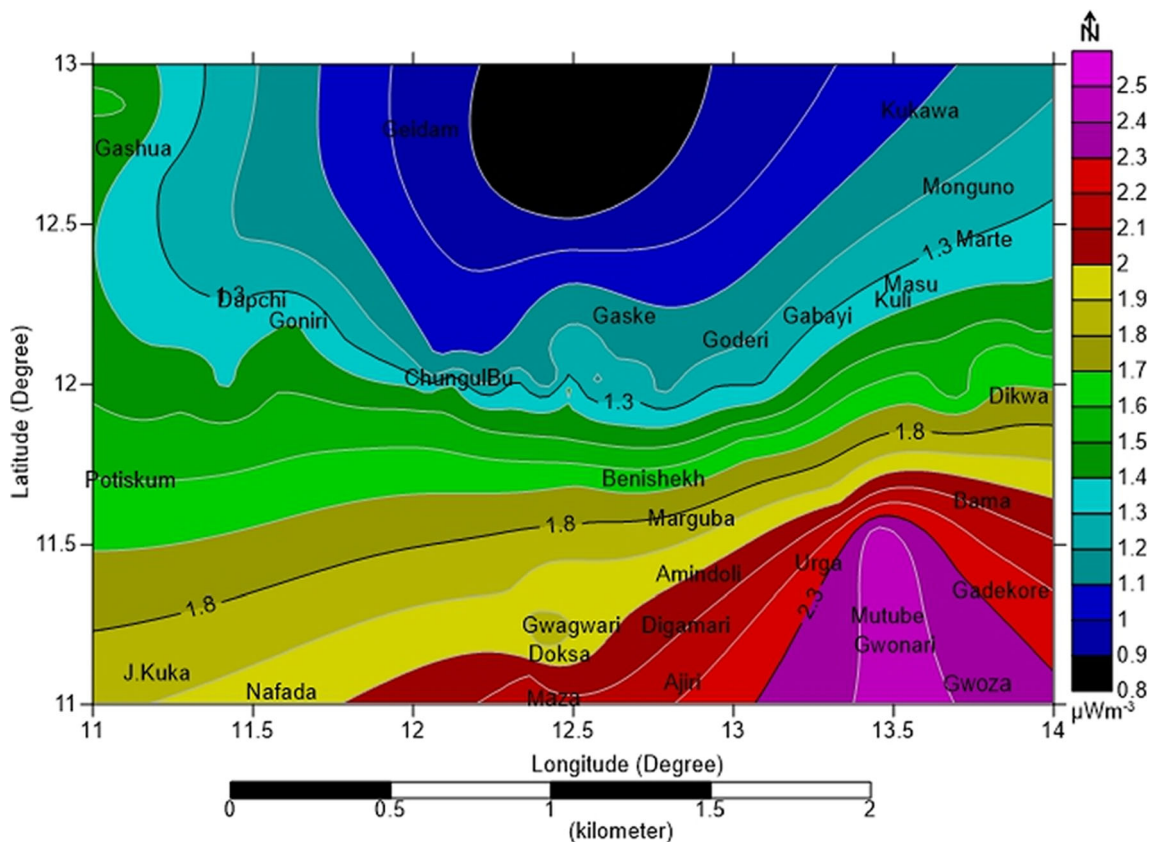
Fig. 8 Contour map of the estimated radiogenic heat flow of the study area

Gwoza and Galdekore has the potential for geothermal exploration.

Integration of aeromagnetic and aeroradiometric data set for potential geothermal exploration

The results from the analysis and interpretation of the airborne magnetic and radiometric data set of Bornu Basin and its environs have revealed the presence of potential geothermal energy within the study area. A close inspection of the heat flow map (Fig. 6f) and radiogenic heat flow (Fig. 7d) shows a very good correlation. The region of maximum heat flow obtained from spectral analysis of aeromagnetic data ranging from 80 to 100 mWm^{-2} agreed with the region of maximum radiogenic heat flow ranging from 2.2 to approximately 2.5 μWm^{-3}, indicating probable geothermal energy within the study area. This agreement between the two heat flows shows that the southeastern part of the study area is a viable source for geothermal exploration within the study area. Just as CPD varies with the geological conditions within the areas of investigation (Ross et al. 2006), so also RHP varies widely with lithology due to variations in the concentration of U, Th, and K (Haack 1982; Čermák and Rybach 1982). The temperature distribution in a sedimentary basin is mainly determined by its formation and evolution processes including the heat flow in its basement (Roque and Ribeiro 1997).

Conclusion

The analysis and interpretation of airborne magnetic and radiometric data of Bornu Basin and its environs have been successfully carried out to assess the heat flow for potential geothermal exploration within the study area on a reconnaissance basis. The combination of the two methods was employed so as to better delineate potential sources for geothermal exploration within the study area.

Results from this study showed that the region of maximum heat flow obtained from spectral analysis of aeromagnetic data ranging from 80 to 100 mWm^{-2} agreed with the region of maximum radiogenic heat flow ranging from 2.2 to approximately 2.5 μWm^{-3}, indicating probable geothermal energy within the study area. The agreement between the two heat flows shows that the southeastern part of the study area is a viable source for geothermal exploration within the study area. It can therefore be stated from this study that integration of airborne magnetic and radiometric methods plays a useful role in geothermal exploration on a reconnaissance basis. The southeastern part of the study area can further be

explored using sophisticated methods for geothermal resources for social-economic development within the study area.

Declarations

Conflict of interest The authors declare that they have no competing interests.

References

Abraham EM, Lawal KM, Ekwe AC, Alile O, Murana KA, Lawal AA (2014) Spectral analysis of aeromagnetic data for geothermal energy investigation of Ikogosi Warm Spring-Ekiti State, southwestern Nigeria. Geothermal Energy 2(1):6

Ademila O, Okpoli CC, Ehinmitan D, (2019) Geological and lithological mapping of part of Igarra schist belt using integrated geophysical methods. Earth Sciences Pakistan (ESP), Zibeline International Publishing, vol. 3(1), pages 1-9

Ademila O (2018) Integrated geophysical methods for subsurface characterisation and health hazard assessment in parts of southwestern basement Nigeria. 2nd International Conference on Science and Sustainable Development, IOP Conf. Series: Earth and Environmental Science. https://doi.org/10.1088/1755-1315/173/1/012024

Adepelumi AA, Falade AH (2017) Combined high-resolution aeromagnetic and radiometric mapping of uranium mineralization and tectonic settings in Northeastern Nigeria. Acta Geophysica 65(5):1043–1068

Aderoju AB, Ojo SB, Adepelumi AA, Edino F (2016) A reassessment of hydrocarbon prospectivity of the Chad Basin, Nigeria, using magnetic hydrocarbon indicators from high resolution aeromagnetic imaging, Ife J Sci 18(2)

Airo ML (2007) Application of aerogeophysical data for gold exploration: implications for the Central Lapland greenstone belt. Geol Surv Finland Spec Pap 44:187–208

Akiishi M, Isikwue BC, Tyovenda AA (2018) Determination of geothermal energy sources in Masu area northeastern Nigeria using spectral analysis of aeromagnetic data. Int J Energy Environ Sci 3(5):89

Alistair TM, Thomas LH, Paul LY, David CW, Alan JC (2014) Gamma-ray spectrometry in geothermal exploration: state of the art techniques. Energies 2014(7):4757–4780. https://doi.org/10.3390/en7084757

Anderson H, Nash C (1997) Integrated lithostructural mapping of the Rössing area, Namibia using high resolution aeromagnetic, radiometric, Landsat data and aerial photographs. Explor Geophys 28(2):185–191

Appiah D (2015) Aeromagnetic and airborne radiometric data interpretation on Chirano area of the Sefwi gold belt, Department of Physics, Kwane Nkrumah University of Science and Technology. (M.Sc. dissertation)

Bansal AR, Dimri VP (2010) Scaling spectral analysis: a new tool for interpretation of gravity and magnetic data. e-J Earth Sci India 3(1):54–68

Bansal AR, Gabriel G, Dimri VP, Krawczyk CM (2011) Estimation of depth to the bottom of magnetic sources by a modified centroid

method for fractal distribution of sources: an application to aeromagnetic data in Germany. Geophysics 76(3):L11–L22

Bassey NE, Barka J (2015) Lithologic and structural mapping using aeromagnetic and ground radiometric data in Song area, NE Nigeria. J Geogr Environ Earth Sci Int 2(4):173–179

Bektaş Ö, Ravat D, Büyüksaraç A, Bilim F, Ateş A (2007) Regional geothermal characterisation of East Anatolia from aeromagnetic, heat flow and gravity data. Pure Appl Geophys 164(5):975–998

Benkhelil J (1989) The origin and evolution of the Cretaceous Benue Trough (Nigeria). J Afr Earth Sci (and the Middle East) 8(2-4): 251–282

Bhattacharyya BK, Leu LK (1975) Analysis of magnetic anomalies over Yellowstone National Park: mapping of Curie point isothermal surface for geothermal reconnaissance. J Geophys Res 80:4461–4465

Bhattacharyya BK, Leu LK (1977) Spectral analysis of gravity and magnetic anomalies due to rectangular prismatic bodies. Geophysics 42: 41–50

Bird DE (1997) Primer: interpreting magnetic data. Am Assoc Pet Geol Explorer 8(5):18–21

Blakeley RJ (1988) Curie temperature isotherm analysis and tectonic implications of aeromagnetic data from Nevada. J Geophys Res 93:817–832

Blakely RJ (1995) Potential theory in gravity and magnetic applications. Cambridge University Press, Cambridge

Čermák V, Rybach L (1982) Thermal conductivity and specific heat of minerals and rocks. In: G Angenheister (ed.), Landolt-Börnstein: numerical data and functional relationships in science and technology, new series, Group V (Geophysics and Space Research), vol Ia, (Physical Properties of Rocks) (pp. 305-343). Springer, Berlin-Heidelberg

Connard G, Couch R, Gemperle M (1983) Analysis of aeromagnetic measurements from the Cascade Range in central Oregon. Geophysics 48(3):376–390

Dieokuma T, Gu HM, Uko ED (2013) Preliminary estimation of thermal conductivity in Bornu-Chad Basin, Nigeria. Eur Sci J 9(30)

Dimgba BC, Obiora DN, Abangwu JU, Ugbor DO (2020) Study of Curie point depth and heat flow from spectral analysis of aeromagnetic data for geothermal potential of Gubio, Chad Basin, Nigeria. SN Appl Sci 2(8):1–9

Ejepu JS, Ako TA, Abdullahi S (2018) Integrated geosciences prospecting for gold mineralization in Kwakuti, North-Central Nigeria. J Geol Min Res 10(7):81–94

Elkhateeb SO, Abdellatif AG (2018) Delineation potential gold mineralisation zones in part of central Eastern Desert, Egypt using airborne magnetic and radiometric data. NRIAG J Astron Geophys 7(2):361–376

Ercan ÖA, Şeren A, Elmas A (2014) Gold and silver prospection using magnetic, radiometry and microgravity methods in the Kışladağ Province of Western Turkey. Resour Geol 64(1):25–34

Eze MO, Mamah LI, Madu AJC, Onuba L (2017) Geological and structural interpretation of possible mineralization zones of part of Anambra Basin and southern Benue trough using airborne geophysical data. Int J Res Eng Appl Sci (IJREAS) Issues 5(7):70–80

Goossens MA (1993) Integrated analysis of Landsat TM, airborne magnetic, and radiometric data, as an exploration tool for granite-related mineralization, Salamanca province, Western Spain. Nonrenew Resour 2(1):14–30

Genik GJ (1992) Regional framework, structural and petroleum aspects of rift basins in Niger, Chad and the Central African Republic (C.A.R.). Tectonophysics 213:169–185

Haack U (1982) Radioactivity of rocks. In: Hellwege K (Ed.), Landolt-Bo˝rnstein numerical data and functional relationships in science and technology. New Series, Group V. Geophysics and Space Research, vol. 1, Physical properties of rocks, supvolume b (pp. 433–481). Springer-Verlag: New York

IAEA (International Atomic Energy Agency) (2003) Guidelines for radioelement mapping using gamma ray spectrometry data, Vienna

Irumhe PE, Obiadi II, Obiadi CM, Ezenwaka CK, Mgbolu CC (2019) Estimating sedimentary pile thickness, structural lineaments and heat flow in parts of North Central Nigeria from aeromagnetic data. Solid Earth Sci 4(3):92–101

Jessop AM, Lewis TJ, Judge AS, Taylor AE, Drury MJ (1984) Terrestrial heat flow in Canada. Tectonophysics 103(1-4):239–261

Joly J (1909) Radioactivity and geology: an account of the influence of radioactive energy on terrestrial history. A. Constable & Company, Limited

Kearey P, Brooks M, Hill I (2002) An introduction to geophysical exploration. Blackwell Science Ltd., London

Kwaya MY, Kurowska E, Arabi AS (2016) Geothermal gradient and heat flow in the Nigeria sector of the Chad Basin, Nigeria. Computational Water Energy Environ Eng 5(02):70

Lawal TO (2020) Integrated aeromagnetic and aeroradiometric data for delineating lithologies, structures, and hydrothermal alteration zones in part of southwestern Nigeria. Arab J Geosci 13(16):1–19

Lawal TO, Nwankwo LI (2017) Evaluation of the depth to the bottom of magnetic sources and heat flow from high resolution aeromagnetic (HRAM) data of part of Nigeria sector of Chad Basin. Arab J Geosci 10(17):1–2

Maden N (2010) Curie-point depth from spectral analysis of magnetic data in Erciyes stratovolcano (Central TURKEY). Pure Appl Geophys 167(3):349–358

Mayhew MA (1982) Application of satellite magnetic anomaly data to Curie isotherm mapping. J Geophys Res 87:4846–4854

Mayhew MA (1985) Curie isotherm surfaces inferred from high-altitude magnetic anomaly data. J Geophys Res 90:2647–2654

NGSA (Nigerian Geological Survey Agency) (2005) Newsletter, volume 2

Nwankwo LI, Shehu AT (2015) Evaluation of Curie-point depths, geothermal gradients and near-surface heat flow from high-resolution aeromagnetic (HRAM) data of the entire Sokoto Basin, Nigeria. J Volcanol Geotherm Res 305:45–55

Nwankwo NC, Anthony AS, Nwosu LI (2009) Estimation of the heat flow variation in the Chad Basin Nigeria. J Appl Sci Environ Manag 13(1)

Nwankwo C, Ekine A (2009) Geothermal gradients in the Chad Basin, Nigeria, from bottom hole temperature logs. Int J Physical Sci 4(12): 777–783

Obaje NG (2009) Geology and mineral resources of Nigeria. Lecture Notes in Earth Sciences. Springer, Heidelberg

Okeyode IC, Olurin OT, Ganiyu SA, Olowofela JA (2019) High resolution airborne radiometric and magnetic studies of Ilesha and its environs, southwestern Nigeria. Mater Geoenviron 66(1):51–73

Okosun EA (1992) Cretaceous ostracod biostratigraphy from Chad Basin in Nigeria. J Afr Earth Sci 14(3):327–339

Okosun EA (1995) Review of geology of Bornu Basin. J Min Geol 31(2): 113–172

Okpoli C, Akingboye A (2016) Reconstruction and appraisal of Akunu–Akoko area iron ore deposits using geological and magnetic approaches. Mater Geoenviron 63(1):19–38

Okubo Y, Graf RJ, Hansent RO, Ogawa K, Tsu H (1985) Curie point depths of the island of Kyushu and surrounding areas Japan. Geophysics 53:481–494

Okubo Y, Matsunaga T (1994) Curie point depth in northeast Japan and its correlation with regional thermal structure and seismicity. J Geophys Res Solid Earth 99(B11):22363–22371

Okubo Y, Tsu H, Ogawa K (1989) Estimation of Curie point temperature and geothermal structure of island arcs of Japan. Tectonophysics 159(3-4):279–290

Okubo Y, Makino M, Kasuga S (1991) Magnetic model of the subduction zone in the northeast Japan Arc. Tectonophysics 192(1-2):103–115

Okubo Y, Matsushima J, Correia A (2003) Magnetic spectral analysis in Portugal and its adjacent seas. Physics Chem Earth, Parts A/B/C 28(9-11):511–519

Olabode SO, Adekoya JA, Ola PS (2015) Distribution of sedimentary formations in the Bornu Basin, Nigeria. Pet Explor Dev 42(5):674–682

Olugbemiro RO, Ligouis B, Abaa SI (1997) The Cretaceous series in the Chad Basin, NE Nigeria: source rock potential and thermal maturity. J Pet Geol 20:51–68

Paoletti V, Pinto A (2005) Aeromagnetic and radiometric data localized filtering at the Vesuvian volcanic area. Boll Geofis Teor Appl 46(2-3):245–259

Pereira LCL, Santos LC, Carrino TA (2019) The role of airborne geophysics in the investigation of gold occurrences in the Itapetim Region, Borborema Province, Northeast Brazil. Braz J Geol 49(3)

Pollack HN, Chapman DS (1977) On the regional variation of heat flow, geotherms, and lithospheric thickness. Tectonophysics 38(3-4):279–296

Reynolds JM (2011) An introduction to applied and environmental geophysics. John Wiley & Ltd. Bans Lane, Chichester, pp 124–132

Ross HE, Blakely RJ, Zoback MD (2006) Testing the use of aeromagnetic data for the determination of Curie depth in California. Geophysics 71(5):L51–L59

Roque A, Ribeiro FB (1997) Radioactivity and radiogenic heat production in the sediments of the São Francisco sedimentary basin, Central Brazil. Appl Radiat Isot 48(3):413–422

Rybach L, Buntebarth G (1981) Heat-generating radioelements in granitic magmas. J Volcanol Geotherm Res 10(4):395–404

Rybach L (1986) Amount and significance of radioactive heat sources in sediments. In: Thermal Modeling in Sedimentary Basins: 1st IFP Exploration Research Conference, Carcans, France, (Vol. 44, p. 311). Editions Technip

Rybach L (1988) Determination of heat production rate. In: Haenel R, Rybach L, Stegena L (eds) Handbook of Terrestrial Heat-Flow Density Determination. Kluwer Academic Publishers, Dordrecht, pp 125–142

Salem A, Ushijima K, Elsiraft A, Mizunga H (2000) Spectral analysis of aeromagnetic data for geothermal reconnaissance of Quseir area, northern Red Sea, Egypt. Proceedings of the world geothermal congress: 1669-1674

Salem A, Green C, Ravat D, Singh KH, East P, Fairhead JD, Biegert E (2014) Depth to Curie temperature across the central Red Sea from magnetic data using the de-fractal method. Tectonophysics 624:75–86

Shirani S, Kalateh AN, Noorollahi Y (2020) Curie point depth estimations for northwest Iran through spectral analysis of aeromagnetic data for geothermal resources exploration. Nat Resour Res 29(4):2307–2332

Siagian ISJ, Nasution BS, Widijono B, Setyanta A, Nurmaliah MK, Adrian N (2013) Airborne magnetic and radiometric geophysical mapping in South and Central Range Mountains, Papua Indonesia. ASEG Extended Abstracts 2013(1):1–4. https://doi.org/10.1071/ASEG2013ab371

Spector A, Grant FS (1970) Statistical models for interpreting aeromagnetic data. Geophysics 35:293–302

Stampolidis A, Kane I, Tsokas GN, Tsourlos P (2005) Curie point depths of Albania inferred from ground total field magnetic data. Surv Geophys 26(4):461–480

Tanaka A, Okubo Y, Matsubayashi O (1999) Curie point depth based on spectrum analysis of magnetic anomaly data in East and Southeast Asia. Tectonophysics 306:461–470

Tsokas GN, Hansen RO, Fytikas M (1998) Curie point depth of the island of Crete (Greece). Pure Appl Geophys 152(4):747–757

Vacquier V (1998) A theory of the origin of the Earth's internal heat. Tectonophysics 291(1-4):1–7

Vilà M, Fernández M, Jiménez-Munt I (2010) Radiogenic heat production variability of some common lithological groups and its significance to lithospheric thermal modelling. Tectonophysics 490(3-4):152–164